


Comprehensive analysis of photonic-crystal surface-emitting lasers via time-dependent three-dimensional coupled-wave theory

Takuya Inoue,^{1,*} Ryohei Morita,² Masahiro Yoshida,² Menaka De Zoysa,¹ Yoshinori Tanaka,¹ and Susumu Noda^{1,2}

¹Photonics and Electronics Science and Engineering Center, Kyoto University, Kyoto-Daigaku-Katsura, Nishikyo-ku, Kyoto 615–8510, Japan

²Department of Electronic Science and Engineering, Kyoto University, Kyoto-Daigaku-Katsura, Nishikyo-ku, Kyoto 615–8510, Japan

 (Received 30 November 2018; revised manuscript received 11 January 2019; published 22 January 2019)

We develop a time-dependent three-dimensional coupled-wave theory (3D-CWT) for the transient analysis of photonic-crystal surface-emitting lasers (PCSELS). Our model takes into account the temporal evolution of both the photon and carrier distribution inside PCSELS, which enable the analysis of various above-threshold lasing characteristics including the relaxation oscillation, spatial hole burning, and multimode lasing. With the developed time-dependent 3D-CWT, we perform transient analysis of the high-power, high-beam-quality PCSELS with double-lattice photonic crystals and reproduce the experimental results of near-field patterns and lasing spectra under high current injection. Our theory enables the comprehensive understanding of the device physics of PCSELS toward the realization of higher-power continuous-wave lasing and short-pulse lasing.

DOI: [10.1103/PhysRevB.99.035308](https://doi.org/10.1103/PhysRevB.99.035308)

I. INTRODUCTION

Photonic-crystal surface-emitting lasers (PCSELS) [1–6] are lasers that use the two-dimensional (2D) band-edge resonant effect of a photonic crystal for both light amplification and surface emission. Owing to their single longitudinal and transverse mode oscillation in two dimensions with a large emission area, PCSELS enable continuous-wave, single-mode lasing with a watt- to ten-watt-class output power and low beam divergence [7–10]. PCSELS also feature flexible functionalities such as the arbitrary shaping of beam patterns and polarizations by the appropriate design of the air-hole patterns [11,12], and on-chip 2D beam steering [13,14].

Along with the above-mentioned experimental progress in PCSELS, the development of analytical tools, which enable accurate analysis of the lasing characteristics of PCSELS, is becoming increasingly important. General computation methods such as the 2D plane-wave expansion method [15] and finite-difference time-domain method [16] cannot be applied to the analysis of PCSELS with large emission areas ($> 300a \times 300a$, where a is the lattice constant of the PC), because the former is only applicable to infinite structures and the latter can treat only small devices such as nano-cavity lasers owing to the requirement of substantial computational resources. To overcome these limitations, we extended the 1D coupled-wave theory originally proposed by Kogelnik and Shank in 1972 [17], and developed a three-dimensional coupled-wave theory (3D-CWT) [18,19] that enables the analytical treatment of the full 3D structure of PCSELS with finite emission areas. In this theory, we focus on the mutual coupling of Bloch waves inside PCSELS, which significantly reduces the computational resources and provides clearer analytical insight for lasing characteristics of PCSELS. Using this theory, we can predict various lasing properties including the threshold gain, mode frequency, far-field pattern, and output

beam polarization. However, our previous work on the 3D-CWT has been restricted to steady-state analysis, neglecting the temporal change of photon and carrier distributions inside PCSELS. The analysis of the transient response of PCSELS, including the rise of the lasing oscillation and mode competition between multiple lasing modes, could not be treated.

In this work, we develop a time-dependent 3D-CWT for the comprehensive analysis of PCSELS by extending the conventional 3D coupled-wave equations into the time domain and combining them with a rate equation for carriers. Our model takes into account both the temporal and spatial evolution of the photon distribution, as well as carrier distribution, inside the PCSELS, and enables a wider range of PCSEL analyses such as relaxation oscillation, spatial hole burning (SHB), and multimode lasing, which cannot be treated with the conventional 3D-CWT. The remainder of this paper is organized as follows. Section II describes the derivations of the time-dependent 3D coupled-wave equations. Section III presents several numerical results of the recently demonstrated high-power high-beam-quality double-lattice PCSEL [8–10] and elucidates the effect of the carrier-induced nonuniformity of the refractive index and gain on the lasing characteristics of PCSELS under high current injection. Section IV concludes this work.

II. DERIVATION OF TIME-DEPENDENT 3D-CWT

Schematics of the cross section and top view of a typical PCSEL device are illustrated in Figs. 1(a) and 1(b), respectively. To derive the time-dependent 3D-CWT, we start with a wave equation for electric field \mathbf{E} , which is obtained by eliminating the magnetic field from Maxwell's equations:

$$\nabla \times \nabla \times \mathbf{E} + \frac{1}{c^2} \frac{\partial^2}{\partial t^2} [\tilde{n}^2(\mathbf{r})\mathbf{E}] = 0, \quad (1)$$

$$\tilde{n}^2(\mathbf{r}) = n^2(\mathbf{r}) + 2in(\mathbf{r})k(\mathbf{r}). \quad (2)$$

Here, c is the speed of light in vacuum, and $n(\mathbf{r})$ and $k(\mathbf{r})$ are the real and imaginary parts of the refractive index,

*t_inoue@qoe.kuee.kyoto-u.ac.jp

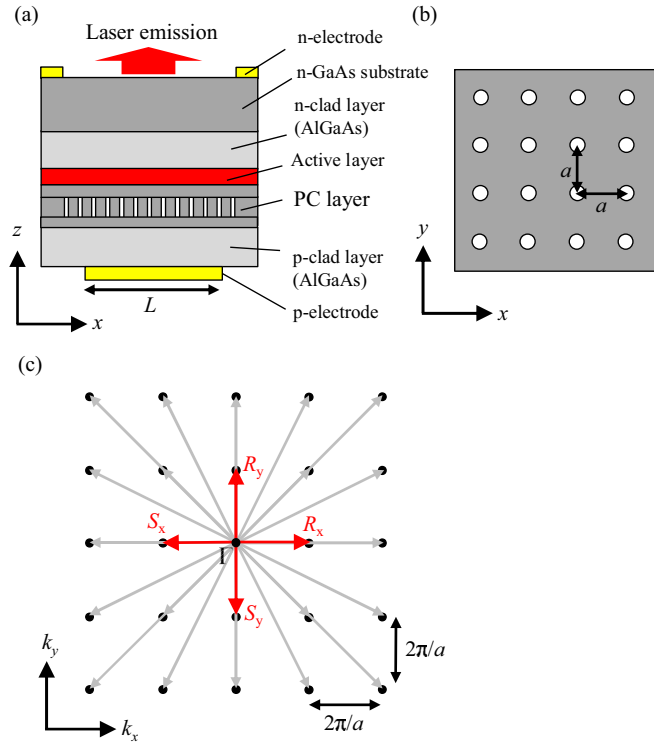


FIG. 1. Schematics of (a) cross-section of a typical PCSEL device and (b) top view of a square-lattice PC. (c) Bloch wave states represented by wave vectors (arrows) in reciprocal space including four basic waves (red arrows), high-order waves, and radiative waves.

respectively. In the case of the square-lattice PC shown in Fig. 1(b), $n^2(\mathbf{r})$ can be expanded as follows:

$$n^2(\mathbf{r}) = n^2(z) + \sum_{(m,n) \neq (0,0)} \xi_{m,n}(z) \exp[-i(m\beta_0 x + n\beta_0 y)], \quad (3)$$

where $\beta_0 = 2\pi/a$ is the length of the primitive reciprocal lattice vector, m and n are arbitrary integers, and $\xi_{m,n}(z)$ is the Fourier coefficient term.

In the case of a steady-state solution for a PCSEL with infinite size, the transverse electric polarization fields $\mathbf{E}(\mathbf{r}, t) = (E_x(\mathbf{r}, t), E_y(\mathbf{r}, t), 0)$ of the Γ -point mode (achieving surface emission) can be expanded according to Bloch's theorem as follows:

$$E_j(\mathbf{r}, t) = \sum_{m,n} E_{j,m,n}(z) \exp[-i(m\beta_0 x + n\beta_0 y)] \times \exp(i\omega_0 t) \quad (j = x, y), \quad (4)$$

where $E_{j,m,n}(z)$ is the z -dependent amplitude of each plane wave and ω_0 is the angular frequency of the resonant mode. In contrast, when we consider the transient response for a PCSEL with finite size, the amplitude of each plane wave gradually changes both temporally and spatially, and can thus be expressed as follows:

$$E_j(\mathbf{r}, t) = \sum_{m,n} E_{j,m,n}(x, y, z, t) \exp[-i(m\beta_0 x + n\beta_0 y)] \times \exp(i\omega_0 t) \quad (j = x, y), \quad (5)$$

where

$$\left| \frac{\partial E_{j,m,n}}{\partial x} \right|, \quad \left| \frac{\partial E_{j,m,n}}{\partial y} \right| \ll \beta_0 |E_{j,m,n}|, \quad (6)$$

$$\left| \frac{\partial E_{j,m,n}}{\partial t} \right| \ll \omega_0 |E_{j,m,n}|.$$

As in the case of the derivation of the steady-state 3D-CWT [18,19], the four basic waves shown in Fig. 1(c) can be expressed as

$$\begin{aligned} E_{x,1,0} &= 0, & E_{y,1,0} &= R_x \Theta_0(z), \\ E_{x,-1,0} &= 0, & E_{y,-1,0} &= S_x \Theta_0(z), \\ E_{x,0,1} &= R_y \Theta_0(z), & E_{y,0,1} &= 0, \\ E_{x,0,-1} &= S_y \Theta_0(z), & E_{y,0,-1} &= 0, \end{aligned} \quad (7)$$

where $\Theta_0(z)$ is the field profile in the z direction, and R_x, S_x, R_y, S_y represent the amplitudes of the basic waves propagating in the $+x, -x, +y,$ and $-y$ directions, respectively. Note that these amplitudes gradually change both temporally and spatially. Substituting Eqs. (3), (5), and (7) into Eq. (1), we obtain the following time-dependent coupled-wave equations in matrix form (the details of the derivation and each symbol are explained in the Appendix):

$$\begin{aligned} \frac{\partial}{\partial t} \begin{pmatrix} R_x \\ S_x \\ R_y \\ S_y \end{pmatrix} &= \frac{c}{n_g} \left[-i\delta + \frac{g - \alpha_{\text{in}}}{2} \right] \begin{pmatrix} R_x \\ S_x \\ R_y \\ S_y \end{pmatrix} - \frac{c}{n_g} \begin{pmatrix} \partial R_x / \partial x \\ -\partial S_x / \partial x \\ \partial R_y / \partial y \\ -\partial S_y / \partial y \end{pmatrix} \\ &- \gamma \begin{pmatrix} R_x \\ S_x \\ R_y \\ S_y \end{pmatrix} + \frac{c}{n_g} \mathbf{C} \begin{pmatrix} R_x \\ S_x \\ R_y \\ S_y \end{pmatrix} + \begin{pmatrix} f_1 \\ f_2 \\ f_3 \\ f_4 \end{pmatrix}. \end{aligned} \quad (8)$$

Here, n_g is the group index of the guided mode, δ is the deviation from the Bragg condition, g is the effective gain for the guided mode (modal gain), α_{in} is the internal material loss, γ is the rate of change of the refractive index, and f is the random noise expressing the spontaneous emission [20]. \mathbf{C} is a 4×4 matrix which represents the cross coupling of the waves shown in Fig. 1(c), including basic, high-order, and radiative waves. The first term on the right side of Eq. (8) denotes the phase rotation and amplification, the second term denotes the spatial propagation of the envelope function, the third term denotes the change in amplitude due to the change in refractive index, the fourth term denotes the cross coupling of the waves, and the last term denotes the spontaneous emission. The output power of the PCSEL can be calculated as follows:

$$P_{\text{rad}}(t) = \iint 2\varepsilon_0 n_{\text{eff}} c \cdot 2\text{imag}(\Phi^t \mathbf{C} \Phi) dx dy, \quad (9)$$

$$\Phi = (R_x, S_x, R_y, S_y)^t.$$

The rate equation for the carrier density $N(x, y)$ inside the active region (multiple quantum wells) can be given by

$$\begin{aligned} \frac{\partial N}{\partial t} &= \frac{J}{ed_{\text{active}}} - \frac{N}{\tau_c} - \frac{c}{n_g} g_{\text{active}} U + D \nabla^2 N, \\ U &= \Gamma_{\text{active}} \frac{2\varepsilon_0 n_{\text{eff}} n_g}{\hbar \omega d_{\text{active}}} [|R_x|^2 + |S_x|^2 + |R_y|^2 + |S_y|^2], \end{aligned} \quad (10)$$

where J is the current density, d_{active} is the thickness of the active layer, τ_c is the carrier lifetime, U is the photon density inside the active layer, D is the diffusion coefficient of the carriers, Γ_{active} is the optical confinement factor in the active layer, and n_{eff} is the effective refractive index of the guided mode. Equation (10) takes into account carrier injection, carrier recombination, stimulated emission, and carrier diffusion. The optical gain of the active layer g_{active} is dependent on the carrier density, which is calculated by considering momentum matrix elements between the wave functions in the conduction and valence bands, their density of states, and the quasi-Fermi energy [21]. For simplicity, in this study, we approximate the gain function of the quantum wells using a linear fractional function of the carrier density with gain saturation [22]:

$$g(N) = \frac{g_{\text{max}}(N - N_{\text{tr}})}{N + [g_{\text{max}}/(-g_0)]N_{\text{tr}}}, \quad (11)$$

where N_{tr} is the transparency carrier density, g_{max} is the saturated gain, and $(-g_0)$ is the absorption coefficient when there are no carriers. It should be noted that the refractive index of the active layer is also dependent on the carrier density, which can be taken into account as the change in the deviation from the Bragg condition δ in Eq. (8).

By solving the time-dependent equations [Eqs. (8) and (10)] simultaneously, the temporal and spatial evolution of both photon and carrier distributions inside the PCSELS can be simulated, enabling transient analyses including relaxation oscillation and short-pulse lasing operation. Unlike the conventional single-mode rate equations for photons, Eq. (8) considers the evolution of all the lasing modes inside the PCSEL simultaneously. When the mode with the lowest threshold gain starts lasing, the carrier density inside the active layer is fixed owing to the stimulated emission term in Eq. (10), which hinders the lasing of the other modes. However, as the spatial distribution of each mode is different, multimode lasing might occur when the threshold gain margin between the fundamental modes and the other modes is small. It should be noted that, in our time-dependent 3D-CWT, the lasing spectra of the PCSEL can be directly calculated by performing a Fourier transform of the transient response of electric fields.

III. NUMERICAL RESULTS

In this section, we apply the above time-dependent 3D-CWT to the transient analysis of the high-power double-lattice PCSEL we recently demonstrated [8–10]. The laser structure to be studied is listed in Table I. A schematic of the PC layer

TABLE I. Structural parameters of the PCSEL.

Layer	Thickness (nm)	Refractive index
n -clad (AlGaAs)	1000	3.122
AlGaAs	80	3.445
Active (InGaAs/AlGaAs)	$(10/20) \times 3$	3.584/3.445
AlGaAs	25	3.269
GaAs	110	3.554
PC	190	n_{ave}
p -clad (AlGaAs)	200	3.297

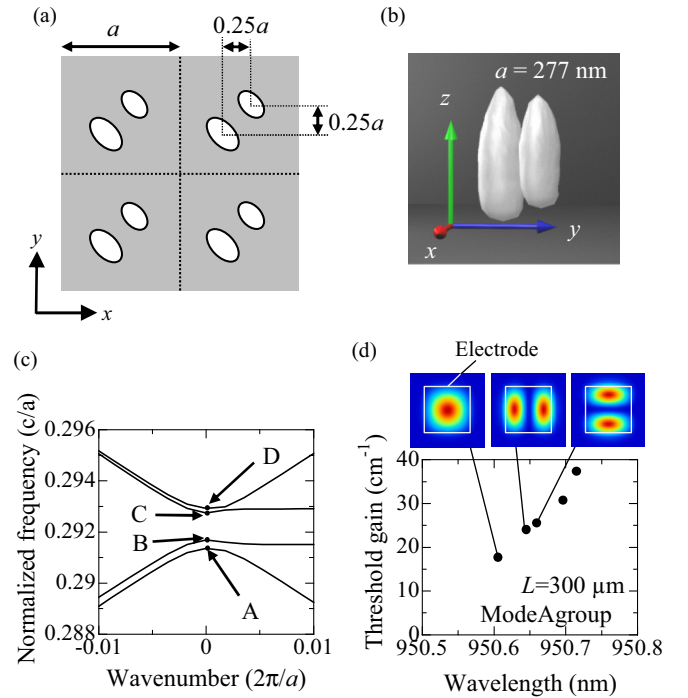


FIG. 2. (a) Schematic of a double-lattice PC. (b) 3D shape of the air holes embedded by MOVPE, which has been reconstructed from scanning electron microscope images. (c) Calculated photonic band diagram near the Γ point. (d) Calculated threshold gain of the fundamental and high-order modes in the mode A group in a device with $L = 300 \mu\text{m}$. The color maps show the photon distributions of the first, second, and third modes, which have been calculated using the conventional 3D-CWT.

is illustrated in Fig. 2(a), which consists of two elliptical air holes with different sizes whose centers of gravity are shifted by $0.25a$ in the x and y directions (referred to as “Structure I” in Ref. [10]). In this structure, light diffracted backward by each air hole destructively interferes, which weakens the confinement of each lasing mode inside the PC. Such weak confinement increases the threshold gain difference between the fundamental mode and the high-order modes and realizes single-mode lasing in a large area [10]. To simulate the fabricated device, we first reconstructed the 3D shape of the air holes embedded by metal organic vapor phase epitaxy (MOVPE) from scanning electron microscope images of the cross section of the holes [shown in Fig. 2(b)], and we then sliced them in the z direction to extract their average refractive index and coupling coefficients. Figure 2(c) presents the photonic band diagram of the fabricated double-lattice PC near the Γ point. Among the four resonant modes at the Γ point, mode A has the lowest radiation constant and thus becomes the lasing mode. Figure 2(d) shows the resonant wavelength and threshold gain of the mode A group in the PC with the finite device size ($L = 300 \mu\text{m}$), which is calculated using the conventional 3D-CWT (carrier distribution is not taken into account). As described above, the destructive feedback by the double holes weakens the optical confinement of the modes and especially increases the losses of the high-order modes, realizing a large threshold gain difference ($\sim 5 \text{ cm}^{-1}$) between the fundamental and high-order modes even at the

TABLE II. Parameters used for 3D-CWT simulations.

Symbol	Parameter	Value
a	Lattice constant	277 nm
n_g	Group refractive index	3.513
n_{eff}	Effective refractive index	3.429
g_{max}	Maximum gain	2000 cm^{-1}
g_0	Absorption coefficient	-5000 cm^{-1}
N_{tr}	Transparency carrier density	$1.5 \times 10^{18} \text{ cm}^{-3}$
α_{in}	Internal material loss	5.0 cm^{-1}
d_{active}	Total thickness of InGaAs wells	30 nm
Γ_{active}	Optical confinement factor	0.044
τ_c	Carrier lifetime	1.5 ns
σ_r	Current spread outside the electrode	$25 \mu\text{m}$
D	Diffusion constant	$100 \text{ cm}^2/\text{s}$
dn/dN	Refractive index change coefficient	$-5.0 \times 10^{-21} \text{ cm}^3$
β	Spontaneous emission factor	1.0×10^{-4}

large device size $L = 300 \mu\text{m}$. It should be noted, however, that the above calculation does not take into account the change in the refractive index and gain induced by carrier injection. Below, we perform comprehensive analysis of the double-lattice PCSEL by using the time-dependent 3D-CWT described in Sec. II. The parameters used in the calculations are summarized in Table II, where we determined the carrier lifetime in the active region τ_c so that the calculated threshold current of the device agrees with the experimental results ($I_{\text{th}} = 0.7 \text{ A}$).

Figure 3(a) presents the calculated temporal change of the carrier density in the center of the electrode (upper) and the output power (lower) at two different current injection levels. After the relaxation oscillation in the beginning of the lasing, both the output power and carrier density converge to a steady-state value, corresponding to continuous-wave operation. The relaxation oscillation frequency of the PCSEL is 1–3 GHz, which increases with the injection current. Figures 3(b) and 3(c) show the spatial distribution of the carrier density and photon density at steady state. Immediately above the threshold current ($I \sim I_{\text{th}}$, left panel), the carrier density inside the electrode is almost uniform while the photons are localized at the center of the electrode. In contrast, at a higher injection current level ($I = 2.8I_{\text{th}}$, right panel), the carrier density in the center of the electrode becomes lower than that near the edge because of a SHB effect. In this case, photons expand toward the edge of the electrode, and the photon distribution becomes more uniform inside the electrode, as shown in the right panel of Fig. 3(c) (the physical explanations are detailed later). Such a change in photon distribution was also observed in the experiment, as shown in the measured near-field patterns of the fabricated PCSEL in Fig. 3(d).

Figure 4(a) shows the calculated lasing spectra of the device at three injection current levels. Here, single-mode lasing with the fundamental mode of the mode A group is achieved at moderate injection levels ($I = 1.4I_{\text{th}}$ and $2.8I_{\text{th}}$), while two-mode lasing with the fundamental and high-order modes is obtained at $I = 4.2I_{\text{th}}$. These results agree with the experimentally measured lasing spectra [9] shown in Fig. 4(c). For comparison, we also performed time-dependent analysis with-

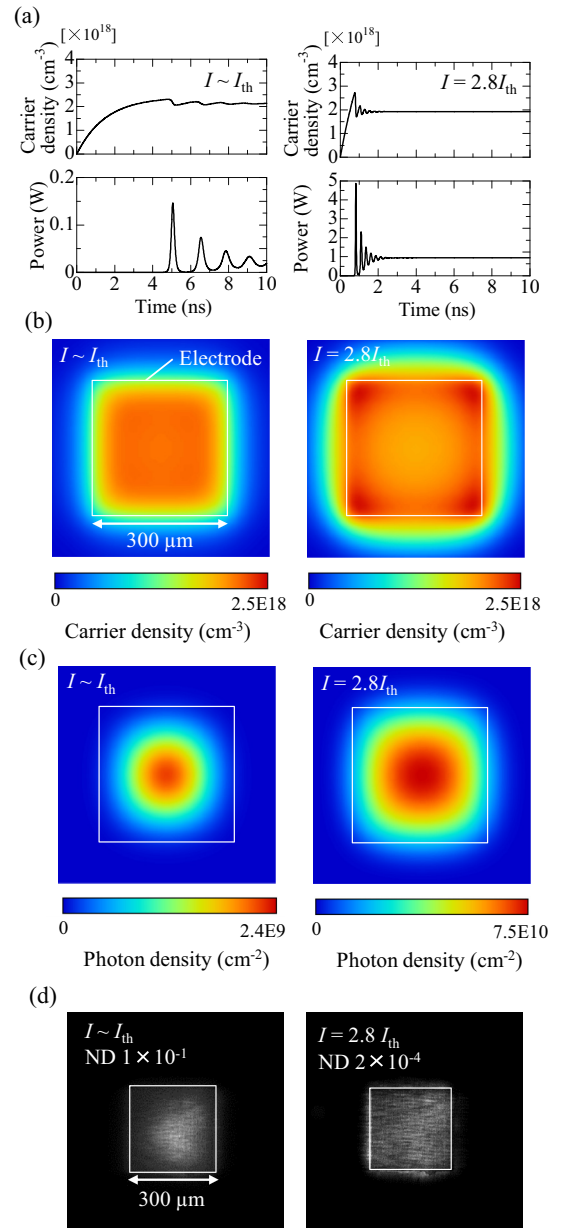


FIG. 3. (a) Calculated temporal change of the carrier density in the center of electrode (upper) and the output power (lower) at two different current injection levels. (b), (c) Calculated carrier density distribution and photon distribution at two different current injection levels, respectively. At the higher injection level ($I = 2.8I_{\text{th}}$), SHB arises in the center of the electrode, and the photon distribution becomes more uniform. (d) Experimentally measured near-field patterns of the double-lattice PCSEL.

out taking into account the carrier-induced refractive index change (only gain distribution is taken into account). The calculated spectra are presented in Fig. 4(b), where single-mode lasing is maintained even at $I = 4.2I_{\text{th}}$. From these results, the cause of the two-mode lasing in our device can be explained as follows. When the current injection level is high, the difference in carrier density inside and outside the electrode becomes large [upper panel in Fig. 4(d)], which induces the spatial variation of the band-edge frequency [lower panel in

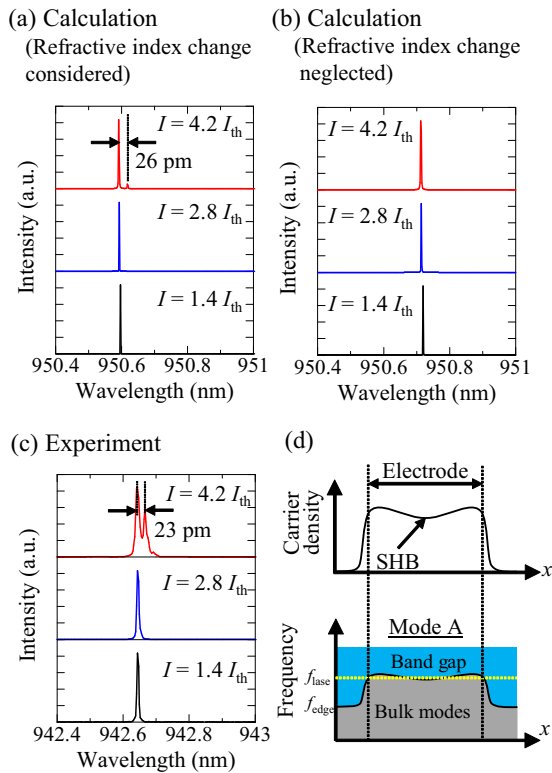


FIG. 4. (a), (b) Calculated lasing spectra of the double-lattice PCSEL at three different injection current levels. The carrier-induced refractive index change is taken into account in (a) but not in (b). The transition from single-mode to two-mode lasing is observed only in (a). (c) Experimentally measured lasing spectra of the fabricated double-lattice PCSEL. (d) Schematic of the spatial distribution of the carrier density (upper) and band-edge frequency (lower). In the case of upward convex band A, a photonic band gap (shown in blue) is formed above the band-edge frequency (f_{edge}), which more strongly confines photons with the lasing frequency (f_{lase}) inside the electrode. A small band gap is also formed in the center of the electrode for photons with f_{lase} , which makes the photon distribution more uniform.

Fig. 4(d)] owing to the carrier-induced change in the refractive index. In the case of the lasing at band A [shown in Fig. 2(c)], which is upward convex, a photonic band gap (shown in blue) is formed above the band-edge frequency (f_{edge}), as shown in the lower panel of Fig. 4(d). As a result, photons with the lasing frequency (f_{lase}) are more strongly confined inside the electrode, which decreases the threshold gain difference between the fundamental and high-order mode. In addition, because of the SHB effect shown in Fig. 3(b), the effective gain for the high-order mode becomes larger than that of the fundamental mode. Such carrier-induced nonuniformity of the refractive index and gain causes the transition from single-mode to two-mode lasing. To maintain single-mode lasing even at a high current injection level, spatial modulation of the injection current or compensation of the carrier-induced refractive index distribution by the spatial modulation of air-hole size might be effective.

It should be noted that, in the lower panel of Fig. 4(d), a small photonic band gap is also formed at the center of the electrode for photons with the lasing frequency (f_{lase}). This small band gap is advantageous for the realization of stable lasing because photons are repelled toward the edge of the electrode, which makes the photon distribution more uniform, as shown in the right panel of Figs. 3(c) and 3(d). On the contrary, for a Γ -point mode at a downward convex band, a photonic band gap is formed below the band-edge frequency (f_{edge}) and photons with the lasing frequency (f_{lase}) are localized at the center of the electrode, which will make the lasing unstable because of the serious SHB effect. Therefore, to maintain stable lasing under high current injection, lasing at band A (upward convex band) is desirable.

IV. CONCLUSIONS

We have developed a time-dependent 3D-CWT in which the temporal evolution of both the photon and carrier distributions inside a PCSEL is self-consistently simulated. Our model takes into account both the temporal change and spatial nonuniformity of the refractive index and gain, enabling a wide range of PCSEL analyses including transient response and lasing spectra, which cannot be treated with the conventional 3D-CWT or single-mode rate equation. By applying this model to the analysis of the high-power double-lattice PCSEL we recently demonstrated, we have reproduced various experimental results including the uniformization of photon distribution and the transition from single-mode to two-mode lasing under high current injection. Although the simulations in this work were applied to a double-lattice PCSEL with a device size of $300 \mu\text{m}$ for continuous-wave operation, our theory can also be applied to the optimization of the radiated output power of double-lattice PCSELs with larger device sizes as well as the transient analysis of PCSELs for short-pulse high-peak-power lasing operation. We believe our time-dependent 3D-CWT will accelerate the comprehensive analysis of PCSELs toward the realization of advanced functionalities including short-pulse lasing as well as single-mode higher-power continuous-wave lasing in PCSELs.

ACKNOWLEDGMENTS

This work was partially supported by the New Energy and Industrial Technology Development Organization (NEDO) and the Cross-Ministerial Strategic Innovation Promotion Program (SIP).

APPENDIX: DETAILED DERIVATION OF TIME-DEPENDENT 3D-CWT

In this appendix, we present a detailed description in the derivation of the time-dependent 3D-CWT [Eq. (8) in Sec. II]. Substituting Eqs. (3) and (5) into Eq. (1) and using Eq. (6),

we obtain

$$\begin{aligned} & \left[\frac{\partial^2}{\partial z^2} + \frac{\omega_0^2}{c^2} n^2(z) + i \frac{\omega_0 n(z) g(z)}{c} - n^2 \beta_0^2 \right] E_{x,m,n} - 2in\beta_0 \frac{\partial E_{x,m,n}}{\partial y} + mn\beta_0^2 E_{y,m,n} \\ & + i\beta_0 \left(m \frac{\partial E_{y,m,n}}{\partial y} + n \frac{\partial E_{y,m,n}}{\partial x} \right) - i \frac{2\omega_0 n^2(z)}{c^2} \frac{\partial E_{x,m,n}}{\partial t} - i \frac{2\omega_0}{c^2} \frac{\partial n^2(z)}{\partial t} E_{x,m,n} \\ & = -\frac{\omega_0^2}{c^2} \sum_{m',n'} \xi_{m-m',n-n'} E_{x,m',n'}, \end{aligned} \quad (\text{A1})$$

$$\begin{aligned} & \left[\frac{\partial^2}{\partial z^2} + \frac{\omega_0^2}{c^2} n^2(z) + i \frac{\omega_0 n(z) g(z)}{c} - m^2 \beta_0^2 \right] E_{y,m,n} - 2im\beta_0 \frac{\partial E_{y,m,n}}{\partial x} + mn\beta_0^2 E_{x,m,n} \\ & + i\beta_0 \left(n \frac{\partial E_{x,m,n}}{\partial x} + m \frac{\partial E_{x,m,n}}{\partial y} \right) - i \frac{2\omega_0 n^2(z)}{c^2} \frac{\partial E_{y,m,n}}{\partial t} - i \frac{2\omega_0}{c^2} \frac{\partial n^2(z)}{\partial t} E_{y,m,n} \\ & = -\frac{\omega_0^2}{c^2} \sum_{m',n'} \xi_{m-m',n-n'} E_{y,m',n'}, \end{aligned} \quad (\text{A2})$$

where $g(z) = 2\omega_0 k(z)/c$ denotes the gain (loss) of the medium. The four basic waves can be expressed as

$$\begin{aligned} E_{x,1,0} &= 0, & E_{y,1,0} &= R_x \Theta_0(z), \\ E_{x,-1,0} &= 0, & E_{y,-1,0} &= S_x \Theta_0(z), \\ E_{x,0,1} &= R_y \Theta_0(z), & E_{y,0,1} &= 0, \\ E_{x,0,-1} &= S_y \Theta_0(z), & E_{y,0,-1} &= 0, \end{aligned} \quad (\text{A3})$$

where R_x, S_x, R_y, S_y represent the amplitudes of the basic waves propagating in the $+x, -x, +y,$ and $-y$ directions, respectively. $\Theta_0(z)$ is the field profile in the z direction, which is assumed to be the same as that of the fundamental guided mode for a multilayer structure in which the PC layer is replaced with a uniform layer having an average refractive index:

$$\begin{aligned} \frac{\partial^2}{\partial z^2} \Theta_0(z) + \left[\frac{n^2(z)\omega_0^2}{c^2} - \beta^2 \right] \Theta_0(z) &= 0, \\ \int_{-\infty}^{\infty} |\Theta_0(z)|^2 dz &= 1. \end{aligned} \quad (\text{A4})$$

Here, β is the in-plane wavenumber of the guided mode. By choosing the appropriate angular frequency ω_0 , we can equate β to β_0 . The effective refractive index of the multilayer structure n_{eff} is defined as $\beta = n_{\text{eff}}\omega_0/c$.

Substituting $(m, n) = (1, 0)$ into Eq. (A2) and using Eqs. (A3) and (A4), we obtain

$$\begin{aligned} & i \frac{2\omega_0 n^2(z)}{c^2} \frac{\partial R_x}{\partial t} \Theta_0(z) \\ & = \left[\beta^2 - \beta_0^2 + i \frac{\omega_0 n(z) g(z)}{c} \right] R_x \Theta_0(z) \\ & - 2i\beta_0 \frac{\partial R_x}{\partial x} \Theta_0(z) - i \frac{2\omega_0}{c^2} \frac{\partial n^2(z)}{\partial t} R_x \Theta_0(z) \\ & + \frac{\omega_0^2}{c^2} \sum_{m',n'} \xi_{1-m',-n'} E_{y,m',n'}. \end{aligned} \quad (\text{A5})$$

Multiplying both sides of Eq. (A5) by $\Theta_0^*(z)$ and integrating with respect to z , we obtain the following time-dependent coupled-wave equation:

$$\begin{aligned} \frac{\partial R_x}{\partial t} &= \frac{c}{n_g} \left(-i\delta + \frac{g}{2} \right) R_x - \frac{c}{n_g} \frac{\partial R_x}{\partial x} - \gamma R_x \\ & + \frac{c}{n_g} \cdot \frac{\omega_0^2}{2\beta_0 c^2} \sum_{m',n'} \int \xi_{1-m',-n'} E_{y,m',n'} \Theta_0^*(z) dz. \end{aligned} \quad (\text{A6})$$

Three more time-dependent coupled-wave equations for S_x, R_y, S_y can be derived in analogous fashion as follows:

$$\begin{aligned} \frac{\partial S_x}{\partial t} &= \frac{c}{n_g} \left(-i\delta + \frac{g}{2} \right) S_x + \frac{c}{n_g} \frac{\partial S_x}{\partial x} - \gamma S_x \\ & + \frac{c}{n_g} \cdot \frac{\omega_0^2}{2\beta_0 c^2} \sum_{m',n'} \int \xi_{-1-m',-n'} E_{y,m',n'} \Theta_0^*(z) dz, \end{aligned} \quad (\text{A7})$$

$$\begin{aligned} \frac{\partial R_y}{\partial t} &= \frac{c}{n_g} \left(-i\delta + \frac{g}{2} \right) R_y - \frac{c}{n_g} \frac{\partial R_y}{\partial y} - \gamma R_y \\ & + \frac{c}{n_g} \cdot \frac{\omega_0^2}{2\beta_0 c^2} \sum_{m',n'} \int \xi_{-m',1-n'} E_{x,m',n'} \Theta_0^*(z) dz, \end{aligned} \quad (\text{A8})$$

$$\begin{aligned} \frac{\partial S_y}{\partial t} &= \frac{c}{n_g} \left(-i\delta + \frac{g}{2} \right) S_y + \frac{c}{n_g} \frac{\partial S_y}{\partial y} - \gamma S_y \\ & + \frac{c}{n_g} \cdot \frac{\omega_0^2}{2\beta_0 c^2} \sum_{m',n'} \int \xi_{-m',-1-n'} E_{x,m',n'} \Theta_0^*(z) dz. \end{aligned} \quad (\text{A9})$$

Here, we define n_g , δ , g , γ as

$$\begin{aligned} n_g &= \frac{\omega_0}{c\beta_0} \int_{-\infty}^{\infty} n^2(z) |\Theta_0(z)|^2 dz, \\ \delta &= (\beta^2 - \beta_0^2) / 2\beta_0, \\ g &= \frac{n_{\text{active}} \omega_0}{c\beta_0} \Gamma_{\text{active}} g_{\text{active}} \left(\Gamma_{\text{active}} = \int_{\text{active}} |\Theta_0(z)|^2 dz \right), \\ \gamma &= \int_{-\infty}^{\infty} \frac{2}{n(z)} \frac{\partial n(z)}{\partial t} |\Theta_0(z)|^2 dz, \end{aligned} \quad (\text{A10})$$

where n_g is the group index of the guided mode, δ is the deviation from the Bragg condition, g is the effective gain for the guided mode (modal gain), n_{active} and g_{active} are the refractive index and gain of the active layer, respectively, Γ_{active} is the optical confinement factor in the active layer, and γ is the rate of change of the refractive index. The last term in Eqs. (A6)–(A9) represents the cross coupling of the waves shown in Fig. 1(c), including basic, high-order, and radiative waves. As is described in our previous papers [18,19], these couplings can be expressed with a 4×4 matrix \mathbf{C} , which directly leads to the derivation of Eq. (8) in Sec. II. It should be noted that the internal material loss α_{in} and the random noise f expressing the spontaneous emission are also included in Eq. (8).

The coupled wave matrix \mathbf{C} can be expressed with the sum of three matrices:

$$\mathbf{C} = \mathbf{C}_{1\text{D}} + \mathbf{C}_{\text{rad}} + \mathbf{C}_{2\text{D}}, \quad (\text{A11})$$

$$\mathbf{C}_{1\text{D}} = \begin{pmatrix} 0 & \kappa_{2,0} & 0 & 0 \\ \kappa_{-2,0} & 0 & 0 & 0 \\ 0 & 0 & 0 & \kappa_{0,2} \\ 0 & 0 & \kappa_{0,-2} & 0 \end{pmatrix}, \quad (\text{A12})$$

$$\mathbf{C}_{\text{rad}} = \begin{pmatrix} \varsigma_{1,0}^{(1,0)} & \varsigma_{1,0}^{(-1,0)} & 0 & 0 \\ \varsigma_{-1,0}^{(1,0)} & \varsigma_{-1,0}^{(-1,0)} & 0 & 0 \\ 0 & 0 & \varsigma_{0,1}^{(0,1)} & \varsigma_{0,1}^{(0,-1)} \\ 0 & 0 & \varsigma_{0,-1}^{(0,1)} & \varsigma_{0,-1}^{(0,-1)} \end{pmatrix}, \quad (\text{A13})$$

$$\mathbf{C}_{2\text{D}} = \begin{pmatrix} \chi_{y,1,0}^{(1,0)} & \chi_{y,1,0}^{(-1,0)} & \chi_{y,1,0}^{(0,1)} & \chi_{y,1,0}^{(0,-1)} \\ \chi_{y,-1,0}^{(1,0)} & \chi_{y,-1,0}^{(-1,0)} & \chi_{y,-1,0}^{(0,1)} & \chi_{y,-1,0}^{(0,-1)} \\ \chi_{x,0,1}^{(1,0)} & \chi_{x,0,1}^{(-1,0)} & \chi_{x,0,1}^{(0,1)} & \chi_{x,0,1}^{(0,-1)} \\ \chi_{x,0,-1}^{(1,0)} & \chi_{x,0,-1}^{(-1,0)} & \chi_{x,0,-1}^{(0,1)} & \chi_{x,0,-1}^{(0,-1)} \end{pmatrix}, \quad (\text{A14})$$

where

$$\kappa_{i,j} = -\frac{\omega_0^2}{2\beta_0 c^2} \int \xi_{i,j} |\Theta_0(z)|^2 dz, \quad (\text{A15})$$

$$\zeta_{p,q}^{(r,s)} = -\frac{\omega_0^4}{2\beta_0 c^4} \iint \xi_{p,q} \xi_{-r,-s} G(z, z') \Theta_0(z') \Theta_0^*(z) dz' dz, \quad (\text{A16})$$

$$\chi_{j,p,q}^{(r,s)} = -\frac{\omega_0^2}{2\beta_0 c^2} \sum_{\sqrt{m^2+n^2}>1} \xi_{p-m,q-n} \varsigma_{j,m,n}^{(r,s)}, \quad j = x, y. \quad (\text{A17})$$

The derivation of the coupled-wave matrix is detailed in our previous papers [18,19]. Here, $\mathbf{C}_{1\text{D}}$, \mathbf{C}_{rad} , and $\mathbf{C}_{2\text{D}}$ correspond to 1D back-diffraction coupling, out-of-plane coupling via radiative waves, and 2D coupling via high-order waves, respectively. $\mathbf{C}_{1\text{D}}$ and $\mathbf{C}_{2\text{D}}$ are Hermitian matrices, while \mathbf{C}_{rad} is not Hermitian, as it corresponds to the power dissipation due to surface emission.

-
- [1] M. Imada, S. Noda, A. Chutinan, T. Tokuda, M. Murata, and G. Sasaki, *Appl. Phys. Lett.* **75**, 316 (1999).
- [2] S. Riechel, C. Kallinger, U. Lemmer, J. Feldmann, A. Gombert, V. Wittwer, and U. Scherf, *Appl. Phys. Lett.* **77**, 2310 (2000).
- [3] M. Imada, A. Chutinan, S. Noda, and M. Mochizuki, *Phys. Rev. B* **65**, 195306 (2002).
- [4] D. Ohnishi, T. Okano, M. Imada, and S. Noda, *Opt. Express* **12**, 1562 (2004).
- [5] M. Kim, C. S. Kim, W. W. Bewley, J. R. Lindle, C. L. Canedy, I. Vurgaftman, and J. R. Meyer, *Appl. Phys. Lett.* **88**, 191105 (2006).
- [6] H. Matsubara, S. Yoshimoto, H. Saito, Y. Jianglin, Y. Tanaka, and S. Noda, *Science* **319**, 445 (2008).
- [7] K. Hirose, Y. Liang, Y. Kurosaka, A. Watanabe, T. Sugiyama, and S. Noda, *Nat. Photonics* **8**, 406 (2014).
- [8] M. Yoshida, M. De Zoysa, R. Hatsuda, Y. Tanaka, K. Ishizaki, and S. Noda, in *2017 Conference on Lasers and Electro-Optics Pacific Rim (CLEO-PR)* (IEEE, Singapore, 2017), pp. 1–3.
- [9] M. Yoshida, M. Kawasaki, M. De Zoysa, Y. Tanaka, K. Ishizaki, R. Hatsuda, and S. Noda (unpublished).
- [10] M. Yoshida, M. De Zoysa, K. Ishizaki, M. Kawasaki, Y. Tanaka, R. Hatsuda, B. Song, J. Gellera, and S. Noda, *Nat. Mater.* (2019), doi:10.1038/s41563-018-0242-y.
- [11] S. Noda, M. Yokoyama, M. Imada, A. Chutinan, and M. Mochizuki, *Science* **293**, 1123 (2001).
- [12] E. Miyai, K. Sakai, T. Okano, W. Kunishi, D. Ohnishi, and S. Noda, *Nature (London)* **441**, 946 (2006).
- [13] Y. Kurosaka, S. Iwashashi, Y. Liang, K. Sakai, E. Miyai, W. Kunishi, D. Ohnishi, and S. Noda, *Nat. Photonics* **4**, 447 (2010).
- [14] S. Noda, K. Kitamura, T. Okino, D. Yasuda, and Y. Tanaka, *IEEE J. Sel. Top. Quantum Electron.* **23**, 4900107 (2017).
- [15] M. Plihal and A. A. Maradudin, *Phys. Rev. B* **44**, 8565 (1991).
- [16] A. Taflov and S. C. Hagness, *Computational Electrodynamics: The Finite-Difference Time-Domain Method, Third Edition* (Artech House, Norwood, MA, 2005).
- [17] H. Kogelnik and C. V. Shank, *J. Appl. Phys.* **43**, 2327 (1972).
- [18] Y. Liang, C. Peng, K. Sakai, S. Iwashashi, and S. Noda, *Phys. Rev. B* **84**, 195119 (2011).

- [19] Y. Liang, C. Peng, K. Sakai, S. Iwahashi, and S. Noda, *Opt. Express* **20**, 15945 (2012).
- [20] P. Vankwikelberge, G. Morthier, and R. Baets, *IEEE J. Quantum Electron.* **26**, 1728 (1990).
- [21] M. Yamada, S. Ogita, M. Yamagishi, K. Tabata, N. Nakaya, M. Asada, and Y. Suematsu, *Appl. Phys. Lett.* **45**, 324 (1984).
- [22] S. Chen, M. Yoshita, T. Ito, T. Mochizuki, H. Akiyama, and H. Yokoyama, *Opt. Express* **21**, 7570 (2013).